VERY LARGE ARRAY–RATAN 600 OBSERVATIONS OF A SOLAR ACTIVE REGION

V. M. BOGOD[1], G. B. GELFREIKH[2], R. F. WILLSON[3], K. R. LANG[3], L. V. OPEIKINA[4], V. SHATILOV[4], and S. V. TSVETKOV[2]

(Received 25 November, 1991; in revised form 3 April, 1992)

Abstract. The Very Large Array (VLA) and the RATAN 600 were used to observe a solar active region on two consecutive days around the time of a partial solar eclipse in July 1990. VLA synthesis maps at 2.0, 3.5, and 6.2 cm wavelength reveal bright ($T_b = 0.2 - 2.2 \times 10^6$ K), compact ($\theta = 10'' - 40''$) sources above the penumbra of the leading sunspot while maps at 20 cm wavelength reveal an extended ($\theta \approx 4.5'$) looplike structure ($T_b \approx 10^6$ K) between the dominant spots. Total flux and brightness temperature spectra of both components were obtained by the RATAN at nine wavelengths between 1.7 and 21 cm. The relatively-flat spectrum of the extended emission is attributed to the optically thin thermal bremsstrahlung of electrons trapped in a magnetic loop at coronal temperatures. Step-spectrum sunspot-associated emission is attributed to thermal gyroresonance radiation at different heights along the leg of a loop joining regions of opposite magnetic polarity. Comparisons with predicted distributions of gyroresonance radiation indicate that the compact sunspot-associated sources lie at heights of $h = 2500 - 17\,500$ km above the photosphere. Although potential fields of sufficient strength appear to exist at coronal heights, differences n the observed and predicted brightness distributions suggest some role for non-potential fields or for an inhomogeneous distribution of electron density or temperature above the sunspot.

1. Introduction

High-resolution VLA observations of the Sun have shown that the microwave emission associated with active regions is often complex, requiring different radiation mechanisms and plasma parameters (e.g., Alissandrakis and Kundu, 1982; Lang and Willson, 1982; Lang, Willson, and Gaizauskas, 1983; Shevgaonkar and Kundu, 1984; Strong, Alissandrakis, and Kundu, 1984; Gary and Hurford, 1987; Nitta *et al.*, 1991; Brosius *et al.*, 1992). At relatively short wavelengths (e.g., $\lambda \leq 6$ cm), the most intense emission is usually located above sunspots where high magnetic fields allow the detection of thermal gyroresonance radiation at coronal heights (Alissandrakis, Kundu, and Lantos, 1980; Lang and Willson, 1982). At longer wavelengths (e.g., 20 cm), the brightest emission often occurs near magnetic neutral lines corresponding to the apex of loops joining underlying sunspots (Lang, Wilson, and Rayrole, 1982; Dulk and Gary, 1983; Lang and Willson, 1983; Lang *et al.*, 1987). Within these higher-lying regions of relatively weak magnetic fields, gyroresonance emission may become insignificant and instead thermal bremsstrahlung dominates.

[1] St. Petersburg Branch of the Special Astrophysical Observatory, Russian Academy of Sciences, St. Petersburg, Pulkovo 196140, Russia.
[2] Central (Pulkovo) Astronomical Observatory Academy of Sciences, St. Petersburg, Pulkovo 196140, Russia.
[3] Department of Physics and Astronomy, Tufts University Medford, MA 02155, U.S.A.
[4] Special Astrophysical Observatory, Russian Academy of Sciences Nizhnij Azchiz, Stavropol Territory 357147, Russia.

Solar Physics **141**: 303–323, 1992.

The brightness and polarization spectrum of thermal bremsstrahlung and gyroresonance radiation depends on the distribution of plasma and magnetic fields within the emitting region. Observations at different wavelengths sample different heights and physical conditions in the solar atmosphere with longer wavelengths referring to higher levels. In some cases, the heights of the microwave sources may be determined from their angular displacements from underlying photospheric features, or else inferred from comparisons with theoretical models which assume a specific temperature and magnetic structure above the active region.

VLA synthesis maps describe the two-dimensional distribution of brightness temperature and polarization, but these data are limited to a few wavelengths in the centimeter and decimeter bands. Moreover, in some configurations, the VLA resolves out extended, low-brightness structures, or 'halos', thereby making it impossible to infer anything about this component of active region emission.

Some of these limitations may be overcome by combining the high angular resolution of the VLA with the broad spectral covarage provided by the RATAN radio telescope. The RATAN provides comprehensive spectral and polarization data that can be used to infer radiation mechanisms and to measure magnetic field strengths at coronal heights (e.g., Krüger *et al.*, 1986; Gelfreikh, Peterova, and Ryabov, 1987). However this instrument can only provide angular resolution in the east–west direction ($\approx 18''$ at 2 cm wavelength) and VLA observations are therefore required to spatially resolve the sources and unambiguously identify them with features on the solar surface. Simultaneous VLA–RATAN observations have, for example, been used to study a type of filament-associated, quiescent radio emission whose high brightness temperature and steep spectrum could not be explained by either thermal bremsstrahlung or thermal gyroresonance radiation (Akhmedov *et al.*, 1986).

In this paper we discuss VLA–RATAN-600 observations of the Sun that took place around the time of a partial solar eclipse in July 1990. The VLA observations were made at wavelengths of 2.0, 3.5, 6.2, and 20.4 cm, while the RATAN observations were made at nine wavelengths between 1.7 and 21 cm.

On the days of our joint observations (21 and 22 July) there were two main active regions (AR 6161 and AR 6162) which had produced a number of flares during the previous several days. We have chosen for this analysis the largest and most complicated of these active regions (AR 6161), located near central meridian. For the first time, VLA images at four wavelengths were compared with one-dimensional scans at the RATAN-600 at the same and additional wavelengths. This made it possible to construct microwave spectra of both sunspot-associated and halo components for the same active region, and to locate these sources with respect to photospheric features. In Section 2 we discuss the radio data and compare them with off-band Hα images and photospheric magnetograms. In Section 3 we use the microwave images and spectra to constrain models of thermal bremsstrahlung and gyroresonance radiation. Our multiwavelength VLA maps are compared with predicted distributions of gyroresonance radiation that were generated using potential field extrapolations together with a model that describes the temperature and density gradient above the active region. Here we show that the magnetic field strengths that are required to explain the sunspot-associated sources are consistent with those inferred from the coronal potential field extrapolations. However, differences in the observed and predicted microwave emission suggest an inhomogeneous distribution of thermal plasma in the corona above the sunspot or the presence of localized flux tubes containing higher density plasma or non-potential fields.

2. Observational Results

2.1. VLA OBSERVATIONS

The VLA was used to observe active region AR 6161 between 18:30–00:30 UT on 21 July, 1990 and between 14:20–21:30 UT on 22 July, 1990. The active region was located at S 28 E21.5 on 21 July and S 28 E07.5 on 22 July. Observations were made in the B configuration at wavelengths of 2.0 cm (14 958 MHz), 3.5 cm (8458 MHz), 6.2 cm (4841 MHz), and 20.4 cm (1471 MHz) on both days. In this configuration the synthesized beamwidths are 0.44″, 0.78″, 1.35″, and 4.5″ at 2, 3.5, 6.2, and 20.4 cm, respectively. The half-power beamwidths of the individual antennas at these respective wavelengths are 3.2″, 5.6″, 9.6″, and 32.6″.

AR 6161 was observed at each wavelength for a period of five minutes, followed by 2-min observations of the calibration source PKS 0552 + 398 every 40 min. In all cases the bandwidth was 12.5 MHz. The data were calibrated with the standard VLA solar calibration routines and then used to produce maps of total intensity I = (RCP + LCP)/2 and Stokes parameter V = (RCP-LCP)/2 at each wavelength. Examination of the fringe visibilities indicated no variations that could be attributed to solar bursts or interference.

In Figures 1 and 2 we show synthesis maps of total intensity for 21 and 22 July. Here we also mark the boundaries of the umbra and penumbra of the leading spot, as determined by co-registering the VLA maps with off-band Hα images from the Mountain Station of the Pulkovo Observatory in Kislovodsk. The uncertainty in the co-registration of the microwave and Hα images is estimated to be $\approx 5''$.

On both 21 and 22 July, the 2, 3.5, and 6.2 cm emission is associated with compact ($\theta = 10''$–$20''$) sources that lie above the eastern edge of the umbra of the leading sunspot. These maps also reveal minor changes in brightness and morphology between the two days of observation, including the emergence of a second 2 cm component (B) and an overall increase in the north–south extent of the 3.5 and 6.2 cm emission. In Table I we give the peak brightness temperature and maximum degree of circular polarization at all wavelengths on both days of observation.

The bright ($T_b \approx 2 \times 10^5$ K), compact ($\theta \approx 10''$) 2 cm sources have a relatively high right-hand circular polarization of ρ_c = 66–85%; the emission at 3.5 and 6.2 cm consists of two or three bright peaks (T_b = 0.9–1.6 × 10^6 K), that have no detectable circular polarization greater than $\approx 20\%$. The sense of the circular polarization at 2 cm corresponds to the extraordinary mode of wave propagation in a magnetic field which has the same polarity as the positive magnetic field of the underlying sunspot (see

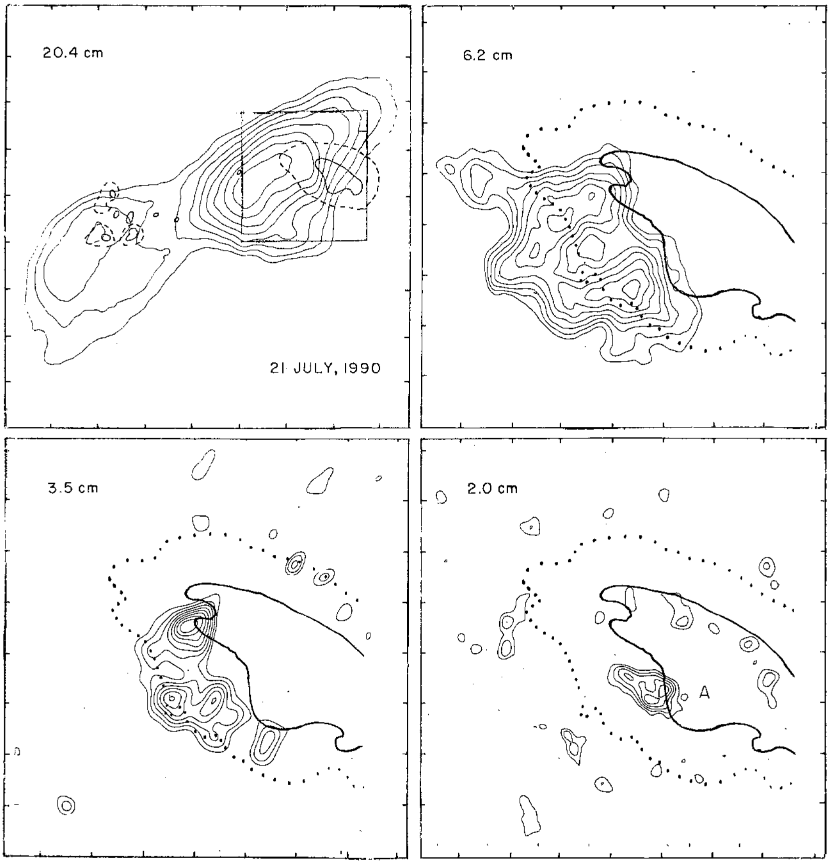

Fig. 1. VLA synthesis maps of total intensity, I, at 2.0, 3.5, 6.2, and 20.4 cm wavelength for active region AR 6161 on 21 July, 1990. The contours mark levels of equal brightness temperature, T_b, with the following outermost contour levels and contour intervals: 2.0 cm: 4.4×10^4 K, 2.3×10^4 K; 3.5 cm: 2.2×10^5 K, 1.1×10^5 K; 6.2 cm: 3.4×10^5 K, 1.7×10^5 K; 20.4 cm: 2.2×10^5 K, 1.1×10^5 K. The fiducial marks on the axes of the 20.4 cm map are drawn at 30″ intervals, with the box denoting the field of view at 2, 3.5, and 6.2 cm. The fiducial marks on these maps are drawn at 10″ intervals, where we also show the boundaries of the sunspot umbra and penumbra.

Figure 3). The peaks of the I and V maps coincide, that is, we find no evidence for any ring-like polarization structure of the type observed by several authors (Alissandrakis, Kundu, and Lantos, 1980; Lang and Willson, 1982; Strong, Alissandrakis, and Kundu, 1984). The peak brightness temperatures of $T_b = 2.2 \times 10^5$ K to 2.2×10^6 K are similar to those found for other quiescent active regions (e.g., Lang, Willson, and Gaizauskas, 1983; Shevgaonkar and Kundu, 1984), suggesting thermal emission at transition region or coronal temperatures.

Figures 1 and 2 show that the emission generally shifts south–eastward, or away, from the leading spot with increasing wavelength (towards the center of the active region). This displacement may be interpreted as a projection effect if the sources at longer

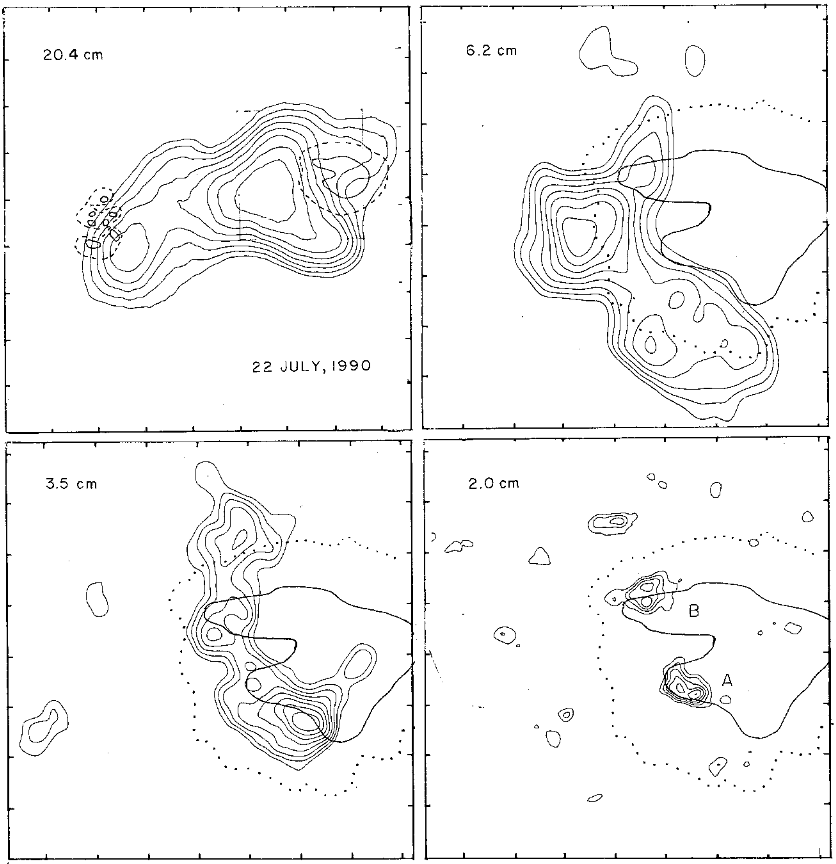

Fig. 2. VLA synthesis maps of total intensity, I, at 2.0, 3.5, 6.2, and 20.4 cm wavelength for active region AR 6161 on 22 July, 1990. The outermost brightness temperature contours and contour intervals are the following: 2.0 cm: 4.4×10^4 K, 2.3×10^4 K; 3.5 cm: 1.8×10^5 K, 9.4×10^4 K; 6.2 cm: 4.4×10^5 K, 2.2×10^5 K; 20.4 cm: 2.0×10^5 K, 1.0×10^5 K. The maps have the same fields of view as those shown in Figure 1.

wavelengths occur at successively greater heights along the legs of loops anchored to the leading sunspot and connecting to the following spots in the east. Similar wavelength–dependent displacements have been observed in other active regions (e.g., Lang, Willson, and Gaizauskas, 1983; Brosius *et al.*, 1992). Coronal potential field extrapolations in fact provide evidence for magnetic loops stretching east-west and connecting the regions of opposite polarity (see Section 3).

Synthesis maps at 20 cm wavelength reveal extended ($\theta \approx 3.8'$) and unpolarized ($\rho_c \leq 10\%$) emission that is contained within a looplike structure lying between the two major spots. This source has two distinct peaks, each lying above the neutral line close to the spots (see Figure 3). On both days, the 20 cm peak associated with the leading spot is the brighter ($T_b \approx 10^6$ K) one. There is no evidence for emission at the shorter wavelengths near this secondary peak with any brightness temperature greater that $T_b = 2 \times 10^5$ K at 3.5 and 6.2 cm and $T_b = 2 \times 10^4$ K at 2 cm.

TABLE I

Parameters of the VLA sources

Date	Wavelength (cm)	T_b (K)	ρ_c (%)
July 21, 1990	2.0	2.3×10^5	≈ 67
	3.5	1.1×10^6	≤ 20
	6.1	1.6×10^6	≤ 10
	20.4	1.1×10^6	≤ 10
July 22, 1990	2.0	2.2×10^5	≈ 85
	3.5	9.4×10^5	≤ 20
	6.1	2.2×10^6	≤ 10
	20.4	1.0×10^6	≤ 10

Fig. 3a.

Fig. 3. The 20.4 cm maps of total intensity are superposed on Kitt Peak magnetograms of AR 6161 on (a) 21 and (b) 22 July, 1990. The most intense emission is associated with the neutral line of the leading spot with more diffuse emission connecting to a secondary peak located close to the following spots. The Kitt Peak magnetograms were kindly provided by Jack Harvey of the National Solar Observatory.

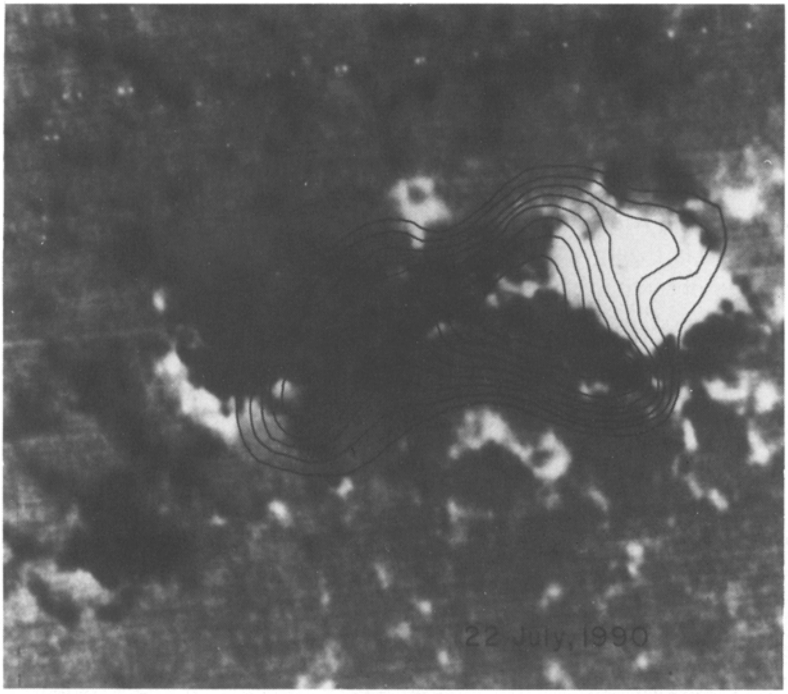

Fig. 3b.

2.2. RATAN-600 OBSERVATIONS

The RATAN-600 was used to observe the Sun on 21 and 22 July, 1990 with five wide-band receivers at wavelengths of 1.7, 2.0, 2.3, 2.7, 3.2, 4.0, 6.0, 11.0, and 21 cm. They were carried out in the 'antenna mode' in which a flat, tiltable reflector or 'periscope' is used to direct the solar radiation toward the southern sector (aperture $\approx 265 \times 5.5$ m) of the primary ring (cf. Khaikin *et al.*, 1972; Parijskij *et al.*, 1976). The signal is then collected by a secondary reflector which focuses the spherical waves onto a set of radiometers operating at different wavelengths. Observations at different azimuths provide fan beam scans in slightly different directions which can be combined to specify the positions of sources on the Sun. The half-power beamwidth at each wavelength is given in Table II.

TABLE II

Half-power beamwidths of the RATAN-600

λ	1.7	2.0	2.3	2.7	3.2	4.0	6.0	11.0	21.0
E–W	15.3″	18.0″	21.0″	25.0″	29.0″	36.0″	54.0″	100″	180″
N–S	10.6′	12.5′	14.4′	16.9′	20.0′	25.0′	37.5′	69.0′	131′

One-dimensional transit records of total intensity, I, and Stokes' parameter, V, were obtained daily around local noon ($\approx 9^h$ UT). On July 22, the center of the beam was directed at the solar center, while on 21 July it was pointed 6′ south of the Sun center. The flux density scale at each wavelength was determined from observations of the Moon and the Crab nebula and absolute coordinate measurements were obtained from observations of 3C84 and 3C273. A detailed description of the RATAN calibration scheme is given by Khaikin *et al.* (1972) and Parijskij *et al.* (1976).

As illustrated in Figure 4, there were two prominent active regions on the Sun during the time of our observations; the one observed by the VLA (AR 6161) is located closer to the central meridian. It should be kept in mind that the fan-beam of the RATAN crosses other active regions along the north–south direction, and that these could potentially contribute to the total signal. However, because these regions appear to be relatively small and diffuse, with weak magnetic fields without sunspots, their contribution to the total flux can probably be neglected.

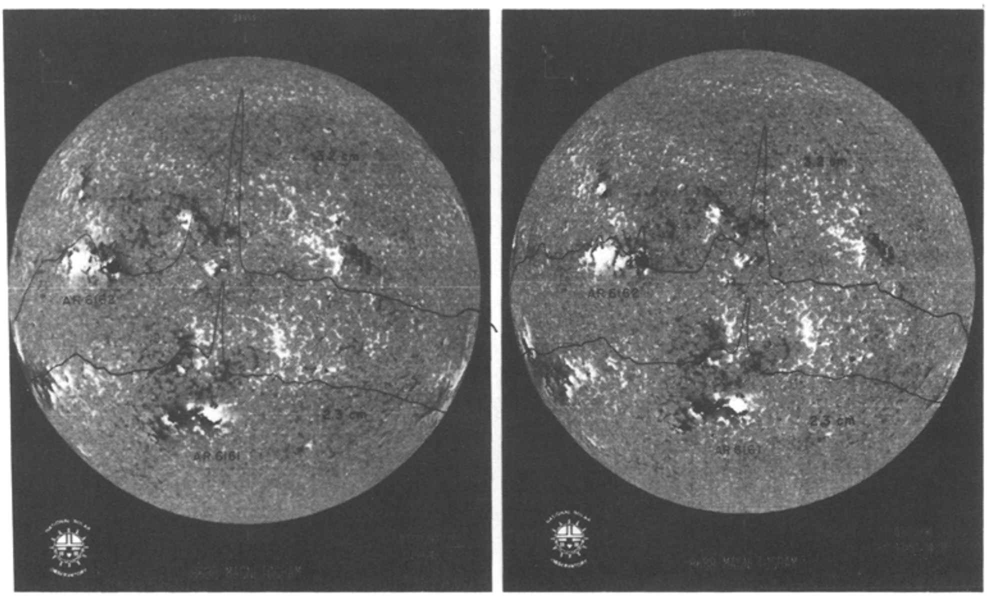

Fig. 4. One-dimensional, full-disk, fan beam scans made at 2.3 and 3.2 cm wavelength with the RATAN 600 on 21 and 22 July, 1990. They are overlaid on Kitt Peak magnetograms taken on the same days. The most intense microwave emission is associated with the active regions AR 6161 and AR 6162 which lie in opposite hemispheres.

High-resolution RATAN observations at the shortest wavelengths (λ = 1.7–4.0 cm) show that the microwave emission consists of three distinct components (Figure 5), that include two relatively compact sources located near the leading and following spots and an extended low-brightness 'halo' between them. The brighter of these compact sources is located near the leading spot with the greatest contrast at 3.2 and 4.0 cm. At 6 cm

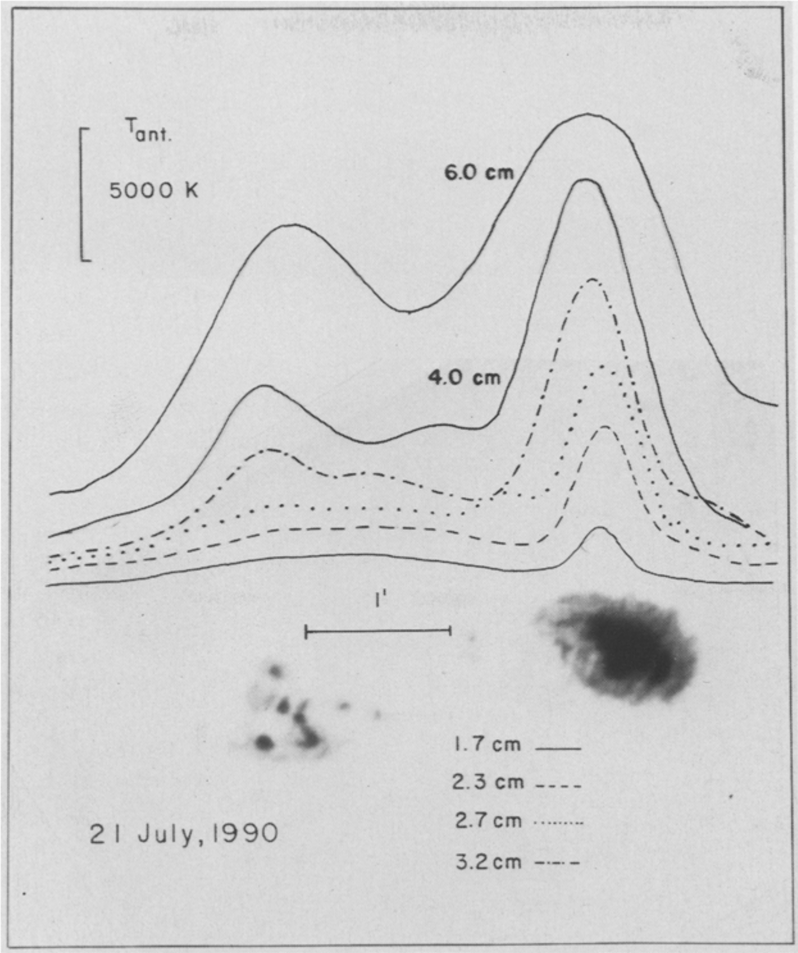

Fig. 5a.

Fig. 5a, b. One-dimensional fan beam scans of AR 6161 taken at six wavelengths with the RATAN 600 on 21 and 22 July, 1990. They are compared with off-band Hα images taken at the Kislovodsk Station of the Pulkovo Observatory. At wavelengths shorter than 2.7 cm, the emission is dominated by a source associated with the leading spot and by an extended halo.

the emission from the leading spot is saturated, while that from the following one increases in intensity, so that these two sources become comparable in flux. The centroid of the stronger sunspot-associated source shifts inward toward the center of the active region with increasing wavelength, in agreement with the VLA results.

The total flux, brightness temperature, angular size and degree of circular polarization size of the dominant sunspot-associated component and the halo at the various wavelengths are given in Table III. These parameters were determined by fitting gaussian functions to the one-dimensional fan beam scans after the data were corrected for the convolution effects of the antenna beam (Parijskij *et al.*, 1976). The brightness tempera-

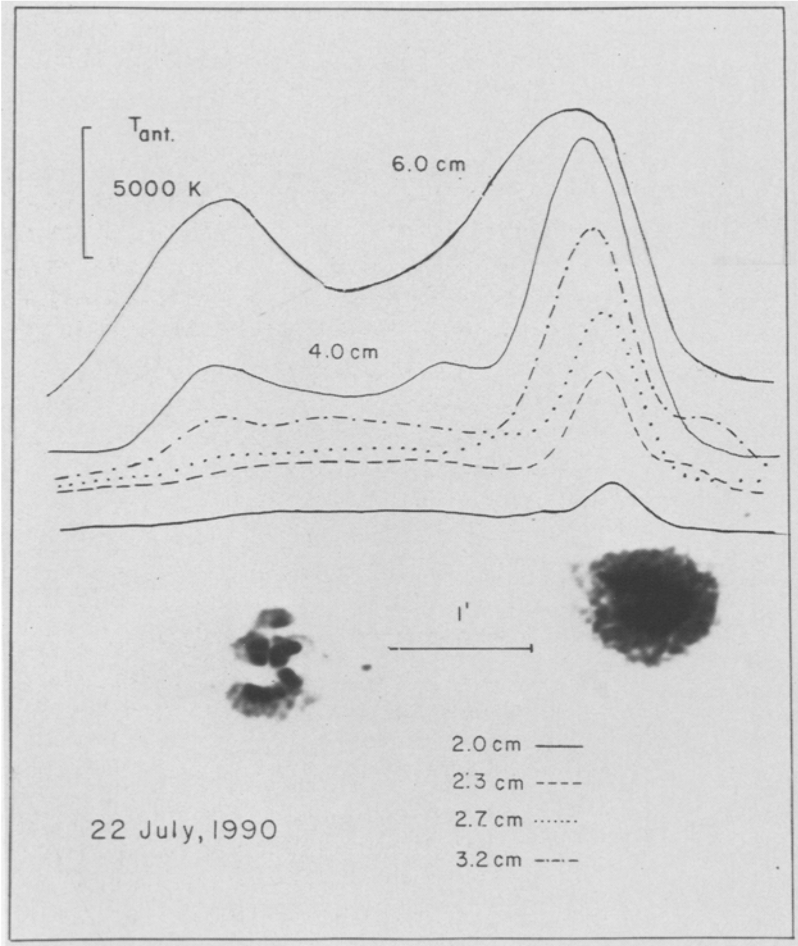

Fig. 5b.

tures were calculated from the total flux by assuming circular symmetry with angular sizes equal to the measured widths. They are consistent with those inferred from the VLA observations and again suggest thermal emission at transition region or coronal temperatures. RATAN observations of other active regions have, for comparison, revealed the presence of sources with brightness temperatures $T_b > 7 \times 10^6$ K, requiring nonthermal radiation mechanisms (Akhmedov *et al.*, 1986).

Because the beamwidths of the RATAN at $\lambda \geq 6$ cm are considerably larger than the angular sizes of the compact sources, the brightness temperatures derived from these measurements have relatively large uncertainties. We have therefore decided to neglect these data in our subsequent analysis.

In Figure 6 we plot the total flux, S_λ, as a function of wavelength for both components. The flux density of the compact source increases with wavelength between 1.7 and 4 cm;

TABLE III

Parameters of the RATAN sources

λ (cm)	Flux (SFU)	T_b (K)	Diameter ($''$)	ρ_c (%)
21 July, 1990				
Spot-associated source (main)				
1.7	1.3	3.3×10^5	13.0	53
2.3	3.5	8.1×10^5	17.5	4
2.7	4.4	9.4×10^5	21.2	3
3.2	6.4	1.2×10^6	26.0	$\leq 3\%$
4.0	6.7	1.3×10^6	33.4	$\leq 3\%$
6.0	10.0	1.1×10^6	66.0	$\leq 3\%$
Halo				
1.7	5.0	1.2×10^4	133.0	$\leq 3\%$
2.3	5.2	2.3×10^4	126.0	$\leq 3\%$
2.7	4.8	3.8×10^4	111.0	$\leq 3\%$
3.2	5.2	5.5×10^4	118.0	$\leq 3\%$
4.0	7.8	6.9×10^4	156.0	$\leq 3\%$
11.0	19.0	9.1×10^5	176.0	$\leq 3\%$
22 July, 1990				
Spot-associated source (main)				
1.7	0.5	2.5×10^5	15.0	53
2.0	1.1	2.8×10^5	15.0	–[a]
2.3	2.6	6.0×10^5	17.5	4
2.7	3.7	9.0×10^5	19.0	4
3.2	5.0	1.3×10^6	23.0	$\leq 3\%$
4.0	5.9	1.9×10^6	25.8	$\leq 3\%$
6.0	6.2	1.8×10^6	50.0	$\leq 3\%$
Halo				
1.7	7.9	0.4×10^5	200.0	$\leq 3\%$
2.0	8.7	0.5×10^5	217.0	$\leq 3\%$
2.3	9.3	0.8×10^5	224.0	$\leq 3\%$
2.7	9.5	1.2×10^5	212.0	$\leq 3\%$
3.2	9.6	1.6×10^5	236.0	$\leq 3\%$
4.0	10.5	2.8×10^5	218.0	$\leq 3\%$
6.0	15.4	9.4×10^5	224	$\leq 3\%$

[a] Circular polarization not observed at this wavelength.

its spectral index, α, ($S_\lambda \sim \lambda^\alpha$) is ≈ 1.5 on 21 July and ≈ 2.5 on 22 July. The emission is strongly polarized at 1.7 cm ($\rho_c \approx 50\%$), decreasing sharply to $\leq 5\%$ at $\lambda = 3.2$ cm. This is consistent with the VLA results which show polarized emission only at 2.0 cm. The spectrum of the halo is unpolarized and is relatively flat ($\alpha \approx 0.0$) at the shorter wavelengths, becoming steep ($\alpha \approx 1.0$–1.5) at $\lambda \geq 4$ cm.

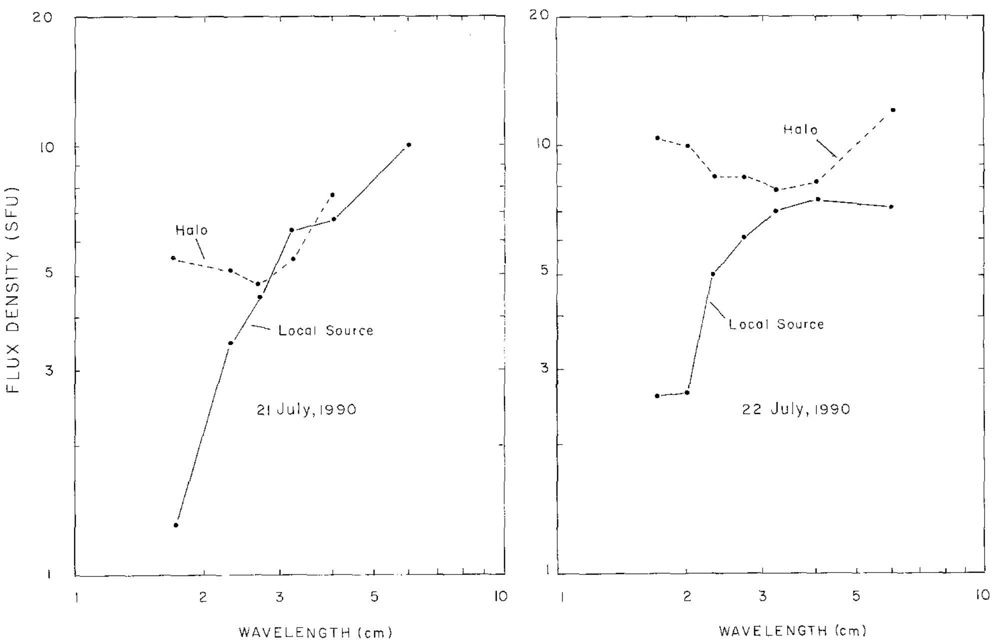

Fig. 6. RATAN flux density spectra for the sunspot-associated and halo components of AR 6161 on 21 and 22 July.

2.3. Magnetic structure and comparisons with optical data

In the bottom half of Figure 5, we show the structure of the sunspots on the two days of observation. Prior to 21 and 22 July, the area of the spots was relatively constant, after which the area of the group declined sharply, reaching another stable configuration for a few more days. Between 19 and 25 July, the maximum umbral fields in the main spot ranged from 2700 to 3100 G as the fields in the following spot remained nearly constant at $\approx$2400 G (*Solnechnye Dannye Bulletin* No. 7, 1990). The magnetic field structure of the entire active region was generally bipolar (see also Figures 3(a) and 3(b)), but had some special features that follow: (1) The positive, or north, polarity of the leading part was confined mainly to the size of the leading spot including the penumbra. (2) In addition to the general bipolar structure, some small islands of negative polarity can also be seen, giving rise to a so-called δ configuration.

From the Kitt Peak magnetogram (Figure 3), it can be concluded that the active region had a well-determined bipolar structure with a dominant leading spot, the trailing flux being divided into several spots with separate or common penumbra. The number of spots or pores between are few and all of negative polarity.

3. Active Region Structure as Inferred from the VLA and RATAN Observations

The RATAN observations (λ = 1.7–6 cm) indicate that the extended halo lies primarily between the spots, encompassing regions of relatively weak ($B_{\max} \leq 1000$ G) photospheric magnetic fields. The size of this source is about 4.5′ in the east–west direction and is comparable to the size of the sunspot group and the flocculae. This extended emission is almost certainly the short-wavelength counterpart of the looplike 20 cm source detected by the VLA. We note that that this extended emission is completely resolved out by the VLA at the shorter wavelengths. In the B configuration, for example, the largest detectable structures have angular sizes of approximately 66″, 38″, and 20″ at 6.2, 3.5, and 2.0 cm, respectively.

The relatively flat spectrum of the halo at $\lambda \leq 6$ cm (Figure 6) may be attributed to the optically thin thermal bremsstrahlung of electrons trapped within loops connecting regions of opposite magnetic polarity. Adopting a coronal electron temperature of $T_e = 2 \times 10^6$ K and using the observed brightness temperature of $T_b = 1.2 \times 10^4$ K at $\lambda = 1.7$ cm, we infer an emission measure of $\int N_e^2 \, dL = 3.4 \times 10^{28}$ cm^{-5}. If we assume a loop thickness of $L = 4.3 \times 10^9$ cm (corresponding to the loop width at the half-intensity level, perpendicular to the major axis), then the electron density is $N_e = [\int N_e^2 \, dl/L]^{1/2} \approx 2.8 \times 10^9$ cm^{-3}. Using this emission measure and extrapolating to longer wavelengths we find a brightness temperature of $T_b = 1.2 \times 10^6$ K at $\lambda = 20.4$ cm, in good agreement with the VLA results (Table I).

The steep spectrum and high circular polarization (at $\lambda = 1.7$ and 2.0 cm) of the sunspot-associated emission is most likely attributed to the thermal gyroresonance radiation of electrons trapped in the leg of the extended loop detected at 20 cm. Previous investigations (e.g., Alissandrakis, Kundu, and Lantos, 1980; Felli, Lang, and Willson; Webb *et al.*, 1987; Lang *et al.*, 1987) have shown that under normal temperatures and densities, the corona above quiescent active regions can remain optically thick up to the fourth harmonic of the gyrofrequency. In this case magnetic field strenghts of $B = 1339$, 765, 432, and 131 G are required at the heights of the 2, 3.5, 6.2, and 20.4 cm 4th harmonic layers.

Because the magnetic field strength above sunspots decreases monotonically with increasing height, gyroresonance emission has been predicted to exhibit a complicated brightness and polarization structure, including wavelength-dependent displacements that depend on the strength and orientation of the field along the line of sight (e.g., Gelfreikh and Lubyshev, 1979; Brosius and Holman, 1989).

The magnetic field structure above the active region was examined by generating a series of potential field extrapolations using photospheric magnetograms from the Big Bear Solar Observatory (courtesy of Haimin Wang and Sara Martin). These calculations used the potential field extrapolation code developed by Sakurai (1982) which solves Laplace's equations to calculate current-free field lines using longitudinal photospheric fields as boundary conditions. This code was also modified to generate maps of the total extrapolated field over a grid of positions all at the same height above the photosphere (see Brosius *et al.*, 1992).

In order to reduce computation time, the 512 × 512 pixel Big Bear images (pixel size = 0.38″ (275 km) × 0.31″ (225 km)) were first averaged over 4 contiguous pixels to give an angular resolution that is comparable to that of the VLA at 6.2 cm. Because these digital magnetograms provide only relative field strengths (H. Wang, private communication), they were calibrated using photospheric magnetic field data obtained from the Kislovodsk Observatory.

In Figures 7 and 8 we show potential field maps at heights of h = 0,5000, 10 000, and 15 000 km above the photosphere. Potential field lines are also drawn in Figures 7(a) and 8(a); they delineate magnetic loops that stretch between the main spots and generally coincide with the extent of the 20 cm VLA emission. Shorter magnetic loops, connecting the spots to nearby patches of weak photospheric flux can also be seen in these figures. The maximum total field strengths, $B = (B_x^2 + B_y^2 + B_x^2)^{1/2}$, at $h = 0, 5000$, 10 000, and 15 000 km are 2705, 1873, 1070, and 763 G on 21 July and 3085, 1934, 1189, and 840 G on 22 July. Our results give vertical magnetic field gradients of $\Delta B/\Delta h \approx 0.2$ G km^{-1} between $h = 0$ and 5000 km. These values are about 35% smaller than those obtained from magnetic field extrapolations of longitudinal fields in the transition region and photosphere of the sunspot umbra of another active region recently studied by Brosius *et al.* (1992).

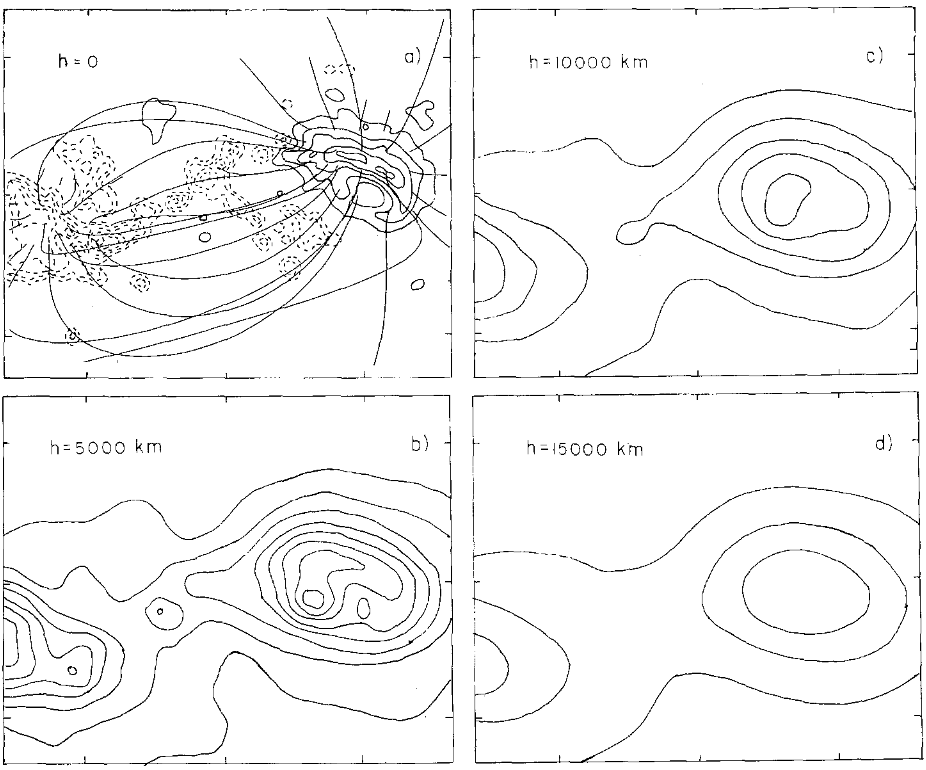

Fig. 7. Contour maps showing extrapolated magnetic field strength at heights of (a) 0 km, (b) 5000 km, (c) 10 000 km, and (d) 15 000 km for 21 July, 1990. The Big Bear magnetogram was taken at 16:31:20 UT. Extrapolated potential field lines are also shown in (a). The fiducial marks are drawn at 60″ intervals. The outermost contour and contour interval of the map in (a) are equal to 500 G; those in (b)–(d) are equal to 200 G. The solid and dashed contours correspond to positive and negative fields, respectively.

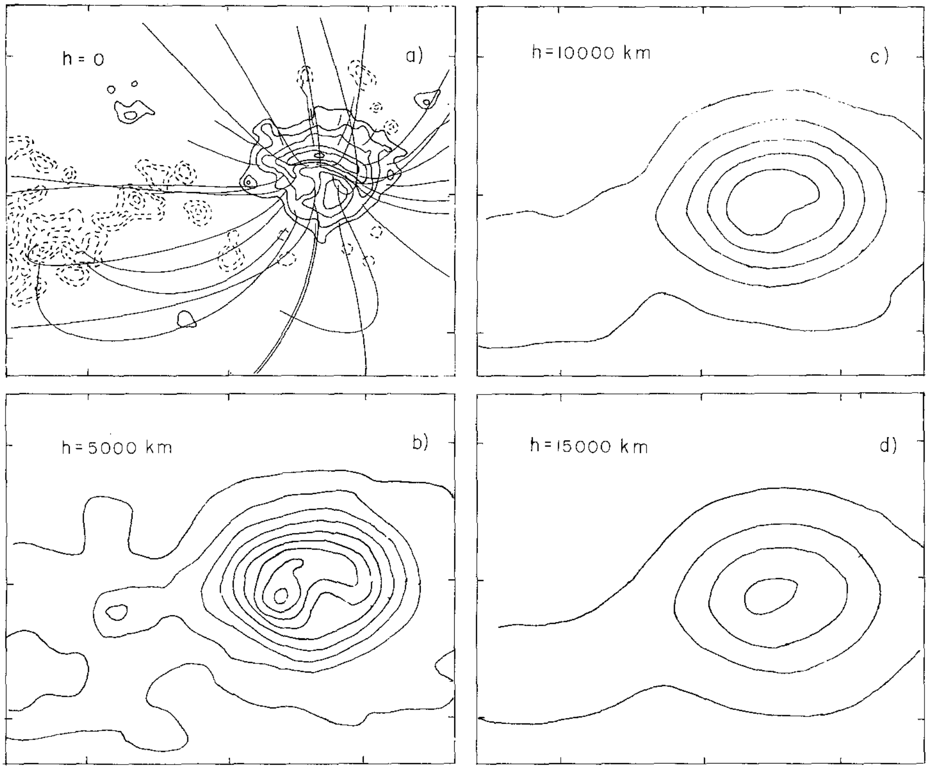

Fig. 8. Same as in Figure 7, but for Big Bear magnetograph data taken at 16:14:41 UT on 22 July, 1990.

If potential fields give an accurate description of the coronal field structure, then these results can be used together with a temperature and density model to predict the distribution of gyroresonance emission at different wavelengths. Comparisons of these theoretical maps with our multiwavelength VLA images may therefore provide insight to the temperature, density and magnetic structure above the active region.

Because of the strong resonant character of gyroresonance absorption, the microwave emission at a given wavelength originates within narrow layers ($\Delta h \approx 1000$ km) where the magnetic field strength corresponds to a given harmonic of the gyrofrequency. The first step in our analysis was therefore to compute the potential fields at heights between 2000 km and 5000 km in steps of 500 km. This range of heights corresponds to the transition region and low corona where the microwave emission is thought to occur. Maps of brightness temperature were then computed by numerically solving the equation of transfer along the line of sight over the 128×128 grid of positions enclosed by the magnetogram. Our calculations used the formula for gyroresonance optical depth, τ_{gr}, given by Dulk (1985) and included contributions from the second, third and fourth harmonics of the gyrofrequency at each height. The optical depth and brightness temperature depend on θ, the angle between the magnetic field and the line of sight, and

$L_H = B/\nabla B$, the magnetic scale length, and these parameters were obtained directly from the potential field calculations.

The gradients of electron temperature and electron density were computed under the assumption of a constant conductive flux in the transition region and corona. In this model, the temperature, T, as a function of height, h, above the photosphere is given by (Alissandrakis, Kundu, and Lantos, 1980)

$$T = (T_0^{7/2} + 3.5F_c(h - h_0)/A)^{2/7}\,, \quad T_0 \leq T \leq T_c\,,$$

where F_c is the conductive flux, T_0 and T_c are the temperatures at the base of the transition region and corona, respectively, h_0 is the height at which $T = \mathrm{T}_0$ and $A = 1.1 \times 10^{-6}$ in c.g.s. units.

The atmosphere above the active region was also assumed to be in hydrostatic equilibrium so that the gas pressure, $P = N_e T$ is given by

$$P = P_0 \exp(-8.9 \times 10^{-11}[T^{5/2} - T_0^{5/2}]/F_c)\,,$$

where $P_0 = 2.0 \times 10^{15}$ cm^{-3} K was taken to be the gas pressure at $h_0 = 2500$ km.

For our calculations we adopted $h_0 = 2500$ km, $T_0 = 2 \times 10^4$ K, and $T_c = 2 \times 10^6$ K, while models were computed for different values of F_c ranging from 5×10^5 to 3×10^7 erg cm^{-3} s^{-1}. These are typical values that have been used in similar model calculations by other authors (e.g., Alissandrakis, Kundu, and Lantos, 1980; Strong, Alissandrakis, and Kundu, 1984; Krüger, Hildebrandt, and Fürstenburg, 1985; Krüger and Hildebrandt, 985; Brosius and Holman, 1989).

In Figures 9 and 10 we compare predicted brightness temperature distributions of total intensity with VLA maps at the same wavelengths. These maps were generated for a constant conductive flux model with $F_c = 2 \times 10^6$ erg cm^{-3} s^{-1} which, from Equations (1) and (2), gives a coronal temperature of $T_c = 2 \times 10^6$ K and an electron density of $N_c = 9 \times 10^8$ cm^{-3} at a height of $h = 20\,000$ km.

The predicted peak brightness temperatures at 2, 3.5, 6.2, and 20.4 cm are, respectively, $T_b \approx 2 \times 10^5$ K, 1.1×10^6 K, 1.8×10^6 K, and 2.0×10^6 K on 21 July and $T_b = 2.3 \times 10^5$ K, 1.4×10^6 K, 1.8×10^6 K, and 2.0×10^6 K on 22 July. These values are in reasonably good agreement with those observed at 2, 3.5, and 6.2 cm (see Table I), while those at 20.4 cm are about a factor of 2 larger than observed.

Our results show that the predicted emission at the shorter wavelengths is confined to the region above and near the main sunspot where the gyroresonance radiation becomes optically thick or nearly optically thick at coronal or transition region temperatures. The source size increases with increasing wavelength because the higher frequency gyroradiation (at a given harmonic) requires higher magnetic fields that are restricted to lower altitudes in the diverging potential field configuration of the sunspot. By calculating the brightness from each thin layer of the model atmosphere, we are also able to determine the height at which the emission at any wavelength originates and to specify the harmonics which contribute to the opacity. These results are summarized in Table IV, where for each wavelength and contributing harmonic, we give the range of height, temperature, and density over which the emission occurs.

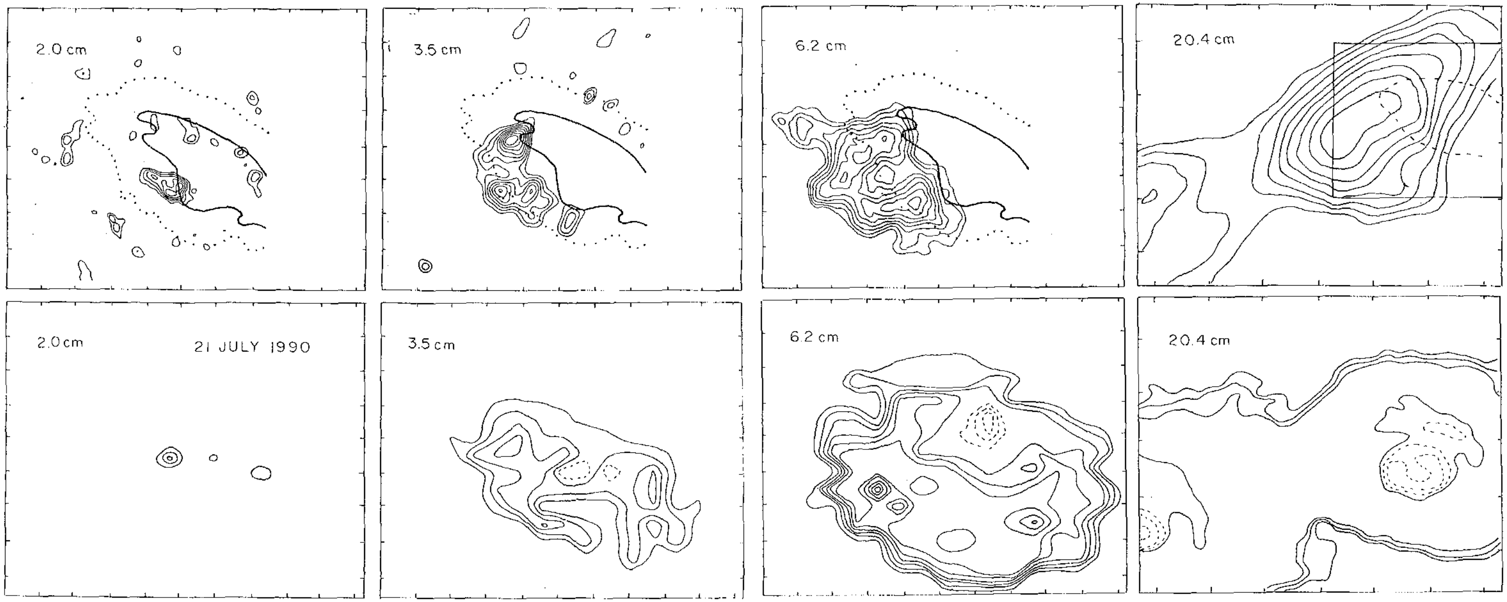

Fig. 9. VLA maps of total intensity, I, are compared with predicted maps of thermal gyroresonance emission on 21 July, 1990. The predicted maps were generated using the potential field extrapolations and a constant conductive flux of $F_c = 2 \times 10^6$ erg cm^{-3} s^{-1}. The brightness temperature contours for the VLA maps are the same as those given in Figure 1. The outermost contour and contour interval of the predicted maps at 2, 3.5, 6.2, and 20.4 cm are equal to 4×10^4 K, 2.5×10^5 K, 2.5×10^5 K, and 5.0×10^5 K. The dashed contours denote depressions below the peak brightness temperatures on the maps and the rectangular box drawn on the 20.4 cm map denotes the field of view of the maps at the other three wavelengths.

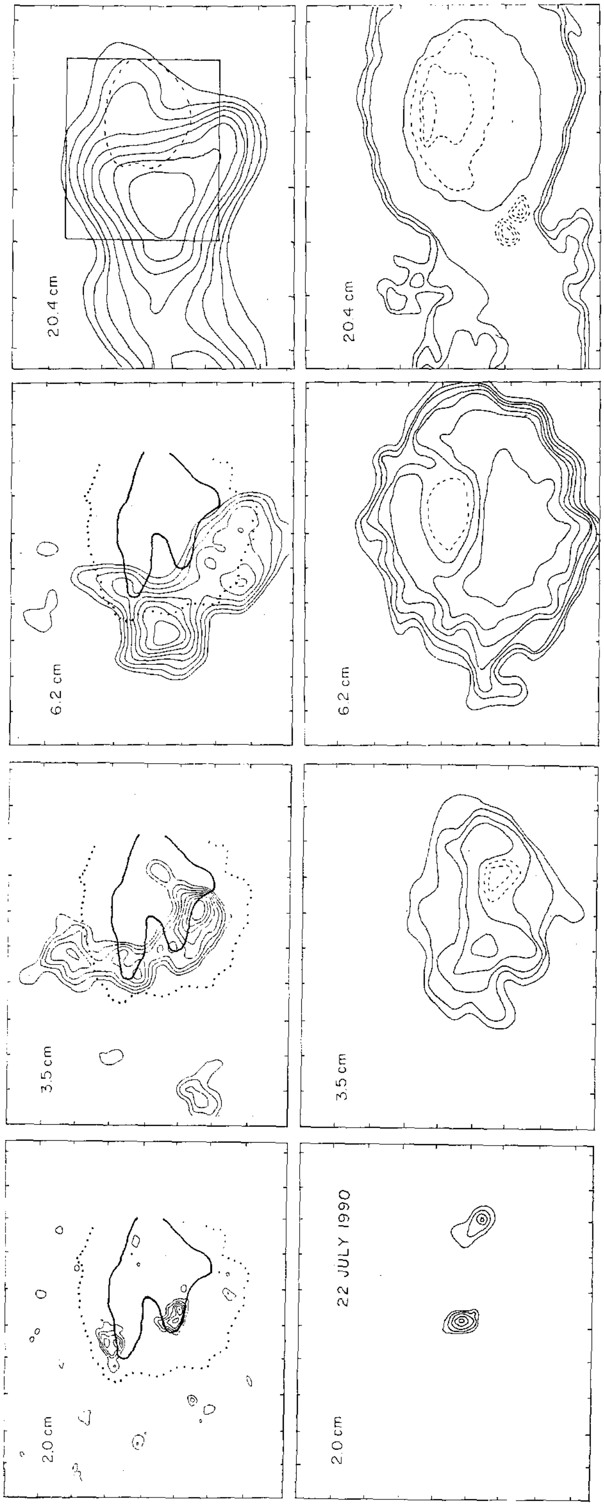

Fig. 10. Same as in Figure 9, but for VLA data taken on 22 July, 1990. The brightness temperature contours of the VLA maps are the same as those given in Figure 2.

TABLE IV

Contributions to the predicted thermal gyroresonance emission

λ (cm)	Harmonic	B (G)	Height (km)	T_e (10^6 K)	N_e (10^9 cm^{-3})
			21 July, 1990		
2.0	3	1785	2500– 3000	0.7–0.9	2.1–2.7
3.5	2	1530	2500– 4000	0.7–1.1	1.7–2.7
	3	1020	3500– 7500	0.9–1.4	1.3–1.9
6.2	2	864	2500–12000	0.7–1.7	0.8–2.7
	3	576	35000–17500	0.9–1.9	0.8–1.9
20.4	2	262	7500–35000	1.4–2.0	0.8–1.3
	3	175	12000– 4000	1.7–2.0	1.0–1.3
			22 July, 1990		
2.0	3	1785	2500– 3500	0.7–1.0	1.9–2.7
3.5	2	1530	2500– 5000	0.7–1.2	1.5–2.7
	3	1020	3500–10000	0.9–1.6	1.1–1.9
6.2	2	864	3500–13500	0.8–1.8	0.9–1.9
	3	576	5000–17500	1.2–1.9	0.8–1.5
20.4	2	262	7500–40000	1.4–2.0	0.8–1.3
	3	175	12000–45000	1.7–2.0	0.8–1.0

Our results indicate that the 3.5, 6.2, and 20.4 cm emission is the superposition of the 2nd and 3rd harmonics, arising at maximum respective heights of $\approx$7500, 17 500, and 40 000 km. The 4th harmonic was found to be optically thin at all wavelengths for the temperature and density model assumed.

The compact 2 cm source is attributed entirely to the 3rd harmonic, corresponding to magnetic fields of $B \approx 1875$ G which lie in the transition region (with T_c within $0.7 - 1.0 \times 10^6$ K) at heights of 2500–3500 km. The 2nd harmonic level ($B = 2627$) lies below the base of the transition region ($h_0 = 2000$ km) and therefore makes no contribution to the brightness. The 2 cm emission is also optically thin ($\tau_{gr} \approx T_b/T \approx 0.2$) resulting in a relatively high degree of circular polarization of $\rho_c \approx 85\%$. Except near brightness temperature depressions above the spot umbra, the 3.5, 6.2, and 20.4 cm emission is optically thick and unpolarized, in agreement with observations.

Increasing the conductive flux from $F_c = 2 \times 10^6$ to 7.5×10^6 erg cm^{-3} s^{-1} increases the peak brightness temperature by factors of $\approx$1.9, 1.5, and 1.1 at 2, 3.5, and 6.2 cm, respectively; decreasing F_c to 5×10^5 erg cm^{-1} s^{-1} decreases T_b by similar factors. This is because larger values of F_c produce narrower transition regions, thereby placing the relevant harmonic levels in regions of higher temperature. Our calculations yield peak brightness temperatures at 2, 3.5, and 6.2 cm that are consistent with the VLA results for $1 \times 10^5 \leq F_c \leq 3 \times 10^5$, suggesting that the transition region above the sunspot in question is relatively thick ($\Delta h_{tr} \approx 20 000$ km). Alissandrakis, Kundu, and Lantos (1980) also found good agreement between theoretical models and 6 cm observations for $F_c = 2 \times 10^6$ erg cm^{-3} s^{-1}. This result, however, has been called into question by Staude (1981) who argued for larger values of F_c.

The maps at all wavelengths show significant brightness temperature depressions ($T_b \leq 5 \times 10^5$ K) above the sunspot umbrae. Such depressions are predicted from the theory of gyroresonant absorption in the magnetic fields of sunspots (Gelfreikh and Lubyshev, 1979); they occur because the angle between the magnetic field and the line of sight above the umbra is small ($\theta \leq 20°$), thereby reducing τ_{gr} and T_b. Near the penumbra, the diverging magnetic field lines cause θ to increase, and the microwave emission becomes optically thick at all heights ($T_b = 2.0 \times 10^6$ K). Although the maps at 3.5 and 6.2 cm show a generally higher concentration of emission above the eastern penumbra, they do not reproduce, in detail, the microwave structure detected at these wavelengths, while also predicting higher brightness temperatures (T_b = 1–2 $\times 10^6$ K) than are observed ($T_b \leq 2 \times 10^5$ K) above the western penumbra.

Gyroresonance maps at 20 cm also indicate optically thick emission over a considerable portion of the active region. The predicted peak brightness temperature of $T_b = 2 \times 10^6$ K is about a factor of 2 higher than is observed, and would seem to suggest (a) an electron temperature of $\approx 10^6$ K at the height where the 20 cm emission becomes optically thick or (b) the presence of cooler, intervening plasma that partially attenuates the hotter loop emission. We note, however, that these maps also predict significantly lower brightness temperatures than are observed at some locations, particularly in the eastern portion of the active region on 22 July and in the depression south of the spot umbra on both days of observation. While we cannot rule out some contribution from gyroresonance radiation, particularly at the peak of the 20 cm source, these differences suggest that thermal bremsstrahlung makes a significant contribution to the brightness of the extended halo source.

Localized peaks of brighter emission at the shorter wavelenghts near the leading spot might be explained by non-potential fields, large magnetic gradients, or narrow flux tubes of hotter, denser plasma emerging into higher layers of the transition region and corona. These features for example, could explain the compact, spatially separated 2 cm sources, *A* and *B*, observed on 22 July. These sources, however, cannot represent the feet of the same magnetic loop, since both exhibit the same sense (RCP) of circular polarization.

The absence of detectable emission above the umbra and western penumbra might also be explained by an inhomogeneous distribution of plasma above the sunspot ; a decrease in the emission measure or electron temperature in the western half of the spot would result in a smaller optical depth and brightness temperature along these directions. For example, in order to produce a brightness temperature of $T_b \leq 2 \times 10^5$, as is observed at 3.5 and 6.2 cm, the electron density in the 2nd harmonic regions must be decreased by a factor of $\approx 10^4$, i.e., to about $N_e \approx 2 \times 10^5$ cm^{-3}. Alissandrakis and Kundu (1980), Strong, Alissandrakis, and Kundu (1982), and Gary and Hurford (1987), for example, explained brightness temperature depressions or asymmetries above sunspots to temperature and/or density deficits in such regions. EUV observations have provided evidence for bright plumes of low temperature gas ($T_e \approx 10^5$ K) above sunspots (Nicolas *et al.*, 1982; Doyle *et al.*, 1985) while comparisons of soft X-ray and 20 cm emitting loops have also suggested the presence of cooler ($T_e \leq 5 \times 10^5$ K) plasma at coronal levels (Lang *et al.*, 1987; Nitta *et al.*, 1991; Brosius *et al.*, 1991). Future VLA and RATAN observations, in combination with simultaneous YOHKOH observations of hot and cool coronal loops, should provide further insight to the distribution of thermal plasma above active regions.

Acknowledgements

Collaborative VLA–RATAN observations of the Sun at Tufts University are supported by the US–Russia Cooperative Research Program of the National Science Foundation under grant ATM 9024506. Radio astronomical studies of the Sun at Tufts University are also supported by NASA grant NAGW-2383 and by grant AFOSR-89-0147 with the Air Force Office of Scientific Research. We are grateful to Haimin Wang, Sara Martin at Caltech and to Jack Harvey at the National Solar Observatory for providing the magnetograms and to T. Sakurai for use of the potential field extrapolation. We also are grateful to the referee for useful suggestions. The VLA is operated by Associated Universities, Inc., under contract with the National Science Foundation.

References

Akhmedov, Sh. B. *et al.*: 1986, *Astrophys. J.* **301**, 460.
Alissandrakis, C. E. and Kundu, M. R.: 1982, *Astrophys. J.* **253**, L49.
Alissandrakis, C. E. Kundu, M. R., and Lantos, P.: 1980, *Astron. Astrophys.* **82**, 30.
Brosius, J. W. and Holman, G. D. 1989, *Astrophys. J.* **342,** 1172.
Brosius, J. W., Willson, R. F., Holman, G. D., and Schmelz, J. T.: 1992, *Astrophys. J.* (to appear).
Doyle, J. G., Raymond, J. C., Noyes, R. W., and Kingston, A. E.: 1985, *Astrophys. J.* **297**, 816.
Dulk, G. A.: 1985, *Ann. Rev. Astron. Astrophys.* **23**, 169.
Dulk, G. A. and Gary, D. E.: 1983, *Astron. Astrophys.* **124**, 103.
Felli, M., Lang, K. R., and Willson, R. F.: 1981, *Astrophys. J.* **247**, 325.
Gary, D. E. and Hurford, G. J.: 1987, *Astrophys. J.* **317**, 527.
Gelfreikh, G. B. and Lubyshev, B. I. 1979, *Soviet Astron.* **23**, 316.
Gelfreikh, G. B., Peterova, N. G., and Ryabov, B. I.: 1987, *Solar Phys.* **108**, 89.
Khaikin, S. E., Kaidanovskii, N. L., Parijskij, Yu. N., and Esepkina, N. A.: 1972, *Isvestia, Main Astronomical Obs. Pulkova*, No. 188, **3**.
Krüger, A. and Hildebrandt, J.: 1986, *Astron. Nach.*, **306**, 157.
Krüger, A., Hildebrandt, J., and Fürstenburg, F.: 1985, *Astron. Astrophys.* **143**, 72.
Krüger, A., Hildebrandt, J., Bogod, V. M., Korzhavin, A. N., Akhmedov, Sh. B., and Gelfreikh, G. B.: 1986, *Solar Phys.* **105**, 111.
Lang, K. R. and Willson, R. F.: 1982, *Astrophys. J.* **255**, L111.
Lang, K. R. and Willson, R. F.: 1983, *Astron. Astrophys.* **127**, 135.
Lang, K. R., Willson, R. F., and Gaizauskas, V.: 1983, *Astrophys. J.* **267**, 455.
Lang, K. R., Willson, R. F., and Rayrole, J.: 1982, *Astrophys. J.* **258**, 384.
Lang, K. R., Willson, R. F., Smith, K. L., and Strong, K. T.: 1987, *Astrophys. J.* **322**, 1035.
Nicolas, K. R., Kjeldseth-Moe, O., Bartoe, J.-D. F., and Brueckner, G. E.: 1982, *Solar Phys.* **81**, 253.
Nitta, N., White, S. M., Kundu, M. R., Gopalswamy, N., Holman, G. D., Brosius, J. W., Schmelz, J. T., Saba, J. L. R., and Strong, K. T.: 1991, *Astrophys. J.* **374**, 374.
Parijskij, Yu. N. *et al.*: 1976, *Soviet Astron.* **20**, 577.
Sakurai, T.: 1982, *Solar Phys.* **76**, 301.
Shevgaonkar, R. K. and Kundu, M. R.: 1984, *Astrophys. J.* **283**, 413.
Staude, J.: 1981, *Astron. Astrophys.* **100**, 284.
Strong, K. T. Alissandrakis, C. E. and Kundu, M. R.: 1984, *Astrophys. J.* **277**, 865.
Webb, D. F., Holman, G. D., Davis, J. M., Kundu, M. R., and Shevgaonkar, R. K.: 1987, *Astrophys. J.* **315**, 716.